IOP Publishing Journal of Physics B: Atomic, Molecular and Optical Physics
J. Phys. B: At. Mol. Opt. Phys. **51** (2018) 035006 (8pp) https://doi.org/10.1088/1361-6455/aa9aa2

Excitation of positronium: from the ground state to Rydberg levels

C J Baker, D Edwards, C A Isaac, H H Telle, D P van der Werf[1] and M Charlton

Department of Physics, College of Science, Swansea University, Singleton Park, Swansea, SA2 8PP, United Kingdom

E-mail: c.baker@swansea.ac.uk

Received 23 August 2017, revised 5 November 2017
Accepted for publication 14 November 2017
Published 12 January 2018

Abstract

Following bombardment of a mesoporous silica sample by positrons ejected from a two-stage buffer gas trap, ortho-positronium (o-Ps) was emitted into vacuum with an efficiency of around 27%–28%. This ensemble, with a density close to 10^{11} m^{-3}, was then irradiated by multiple solid state-based laser beams up to 50 ns after positron implantation. Tunable over a wide range (230–2200 nm), the lasers have enabled excitation of the o-Ps Lyman-α transition, followed by subsequent excitation and, if desired, ionisation to vacuum. Excitation from the 2P state to intermediate states in the principal quantum number, $n_{\rm Ps}$, range $3 \leqslant n_{\rm Ps} \leqslant 18$ has been achieved with efficiencies $\epsilon_{\rm ex}^{n_{\rm Ps}} \gtrsim 80\%$, whilst the excitation efficiency of ground state o-Ps to the 2P state of $\epsilon_{\rm ex}^{2} \sim 13\%$ is currently limited by a mismatch between the Doppler broadening of the 1S-2P transition and the 225 GHz laser bandwidth at 243 nm.

Keywords: antimatter, positron, positronium, spectroscopy, Rydberg

(Some figures may appear in colour only in the online journal)

1. Introduction

Since its existence was postulated by Mohorovičić in 1934 [1] and its subsequent observation by Deutsch in 1951 [2], positronium (Ps), the bound state of a positron (e^+) and an electron, has been the subject of numerous studies. As the simplest matter-antimatter atomic system it has been investigated in various ways, for instance spectroscopically (see, e.g., [3–7]), via its scattering from atoms and molecules (see, e.g., [8–10]) and as a result of its use as a probe in materials analysis (examples include, [11–13]). It has also been suggested as a means of investigating the gravitational behaviour of antimatter [14–16] and has, and will, find application as an intermediary in the production of anti-hydrogen [17–26].

While its formation from beams of low energy e^+s can be relatively efficient (typically 10%–100%, dependent upon circumstances), the limited strengths of laboratory-based β^+ sources (which result in useful beam intensities typically up to a few Me^+ s^{-1}), and the availability of suitable wavelength continuous lasers, has limited the scope of the investigations that have previously been performed. However, Cassidy *et al* [27] recently combined advances in positron traps with proven dye laser technology to produce high intensity pulsed beams which enabled excited states of Ps to be formed and studied. Here we report upon the simplification of these techniques to efficiently produce Ps in principal quantum states $2 \leqslant n_{\rm Ps} \leqslant 18$ via the use of a two-stage buffer gas trap and a commercial solid state laser system which requires minimal user expertise. Our work has also involved the estimation of excitation efficiencies, a preliminary analysis of the observed linewidths of the excited states and a discussion of near-threshold photoionisation.

In the following section the experimental apparatus is described and its typical operating parameters characterised. In sections 3–6 the main experimental results are presented and discussed, whilst section 7 presents our conclusions with associated remarks.

[1] Current address: IRFU, CEA, University Paris-Saclay, F-91191, Gif-sur-Yvette Cedex, France.

2. Experimental apparatus

2.1. Positrons

The main features of the experimental apparatus, which is comprised of the two-stage positron accumulator and the laser system, have been described in detail elsewhere [28, 29] and will only be highlighted here.

A sealed 0.55 GBq ^{22}Na radioactive source located behind an inverted copper cone was placed in thermal contact with, but electrically isolated from (using a sapphire disk), a Sumitomo GM cold head held at around 5.7 K. This was exposed to ultra-pure neon gas for approximately 30 min for positron moderator growth (see, e.g., [30, 31]). The neon pressure within the vacuum chamber, whose base pressure was $<1 \times 10^{-10}$ mbar as measured by a compact cold cathode gauge, was stabilised at 2×10^{-3} mbar via a PID controlled piezoelectric valve. This procedure enabled the establishment of a rare gas moderator which resulted in $\sim 2.5 \times 10^{6}$ low energy positrons per second being guided approximately 1.5 m downstream to a closed, inline, isolation gate valve by an axially aligned 10–50 mT magnetic field.

During neon condensation onto the source and copper cone the number of low energy positrons able to reach the gate valve, after traversing a crude magnetic field-based energy selector, was monitored by detecting the resulting 511 keV annihilation gamma-rays using a CsI-photodiode detector. This detector was operated in the single gamma-ray counting mode, and its efficiency calibrated using ^{22}Na and ^{60}Co test sources of known activity. This allowed the neon plating (corresponding to the moderator growth) time and deposition pressure to be optimised, subject to apparatus constraints.

Once the moderator was established and the pressure within the source chamber had returned to background levels, the inline valve was opened to permit the positrons into the experimental regions. In order to produce the required high intensity positron pulse a two-stage buffer gas accumulator, with a design optimised for 10 Hz operation [28], was employed. The first stage of the instrument was comprised of fifteen gold-plated cylindrical electrodes of 16 mm inner diameter and 24 mm length assembled in a long cylinder, and suitably electrically biased to form a potential well. Molecular nitrogen gas was injected at the mid-point to establish a pressure of approximately 10^{-3} mbar inside the device, such that energy loss of positrons via an inelastic collision (electronic excitation of the nitrogen) occurred with a high probability to effect trapping. However, due to the high pressure the likelihood of positron annihilation (with lifetimes of the order of 0.1s) was prohibitive; therefore five further electrodes of inner diameter 41 mm and length 49 mm were attached immediately after this stage to form a second stage. As a result of the larger electrode diameter, and the attendant increase in pumping speed, the pressure here was reduced to approximately 10^{-4} mbar. Biasing of the electrodes resulted in the axial confinement of those positrons that had undergone at least one inelastic collision, and subsequent collisions resulted in their accumulation in a ~10 mm long region of the second stage. Radial confinement was provided by a 35 mT axial magnetic field, but positron-molecule collisions and field inhomogeneities caused deleterious radial drifts [32, 33]. To counteract this, the axial position of the accumulated positron ensemble was chosen such that appropriately phased, time-dependent, potentials applied to an azimuthally segmented electrode resulted in radial compression via the so-called 'rotating-wall' technique [34, 35]. To facilitate this (indeed it is a requirement in our system) small quantities of a second cooling gas (typically CF_4) were admitted into the vacuum chamber near the second stage with a partial pressure estimated to be 10^{-6} mbar.

For the studies reported here, the system was operated at a rate of 1 Hz in order to increase the number of Ps atoms formed and to enhance signal-to-noise to aid in their detection (see section 3). This operation resulted in clouds of around 3×10^{5} positrons of radius ~1 mm and with densities close to 10^{13} m^{-3}. Coincidentally, this operation mode also aided the reliability of the excited Ps production by ensuring maximum laser power availability prior to interaction with the Ps ensemble. This was achieved by pulse-picking from the free-running (10 Hz, see section 2.2) laser in a manner which was synchronous with the generation of the Ps pulse (see below).

Once released from the accumulator, via the removal of the potential on the exit electrode in around 10 ns, the positrons were magnetically guided further downstream, first through a 38 mm diameter, 320 mm long, pumping restriction (the magnetic field at which point was increased to 0.1 T to minimise losses) and into another assembly of nineteen, 41 mm diameter, cylindrical electrodes, forming a third trapping stage. These electrodes have differing lengths along the trap in order to maximise, when they are appropriately electrically biased, the harmonicity of the resulting potential well, though this feature was not implemented for the present studies. However, three of the electrodes of this assembly have been successfully used to produce an approximately linear 10 V cm^{-1} electric field for 10 ns, which temporally compressed the positron cloud from ~30 to ~4 ns FWHM (as deduced from fitting to the gamma-ray timing spectra as described in section 3) at the Ps production target 2 m downstream to better match the temporal characteristics of the laser system.

Following the third-stage the positrons passed through a further valved pumping restriction of length 220 mm and diameter 38 mm to enter the Ps production and laser beam interaction region. This was formed inside a standard six-way DN160 vacuum cross that contained, as shown in figure 1, a silica sample [36] mounted on an electrically isolated target with a grid and an electrode plate that could be independently biased.

2.2. Lasers

Two laser systems were employed to promote positronium to the desired level as illustrated in figure 2; the first was used to excite ground state ortho-positronium to the 2P state with the

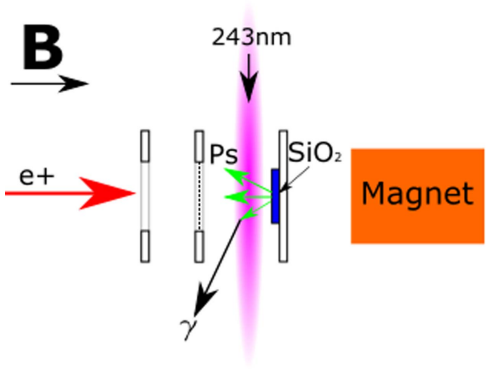

Figure 1. Schematic illustration (not to scale) of the target area with the silica sample (blue) held on a backing plate. The positron pulse, confined radially by the axial magnetic field, **B**, was directed onto the target. The laser beams passed between the target and an electrically isolated grid, with the burst of annihilation gamma-rays detected by a $PbWO_4$ scintillator–phototube arrangement (not shown) located external to the vacuum chamber. A Nd permanent magnet was used, located around 1 cm behind the sample, in some of the studies (see text for details).

second providing access to a subsequent, higher, level and then to ionise, when required.

The details of the system for the first excitation step, at a wavelength λ_{UV}, have been published previously [29] and remain largely unchanged. In essence light of wavelength 243 nm was obtained using a commercial 10 Hz Nd:YAG system, with an internal second harmonic generator set to deliver 500 mJ of 1064 nm (1ω) and 280 mJ of 532 nm (2ω) light in a 12 ns pulse. These two beams were directed into a deuterated potassium dihydrogen phosphate third harmonic generator to produce 40 mJ of 355 nm (3ω) within a 10 ns pulse. The remaining 532 nm beam was used to pump a commercial optical parametric oscillator (OPO) set to deliver a 770 nm signal wave with an energy of 25 mJ in an 8 ns pulse. The 355 and 770 nm beams were then directed into a sum frequency generator containing a 7 mm long Beta Barium Borate (BBO) crystal which resulted in up to 1.5 mJ of the desired 243 nm output in an 8 ns pulse with a linewidth of 225 GHz. The automated mechanical variation of the two BBO crystals within the OPO permitted a 2 nm tuning range to be accessed and this, along with the 6 mm diameter of the laser pulse within the interaction region, ensured good overlap both with the spatial and the Doppler broadened wavelength profiles of the emitted Ps cloud. The wavelength was continuously monitored by an Ocean Optics HR4000 wavemeter.

The second excitation step required a laser system tunable over a much larger range in order to address a number of Ps states. To achieve this the 2ω output from a second Nd:YAG was directed into a further identical OPO which permitted up to 60 mJ of light from 680 to 2200 nm to be produced and directed through CaF_2 windows into the vacuum chamber, following the selection of the idler or signal wave via a glan polariser. This second laser pulse was typically also 8 ns in duration (as measured by a Thorlabs SV2-FC photodiode detector) and of $\sim$6 mm diameter (as measured by the simple 'burn-paper' damage threshold method). Reflections of the selected wavelength were continuously monitored on a calibrated High Fineness Angstrom WS-6D LC wavemeter to ensure wavelength and power stability of 1 part in 10^6 and 3% respectively.

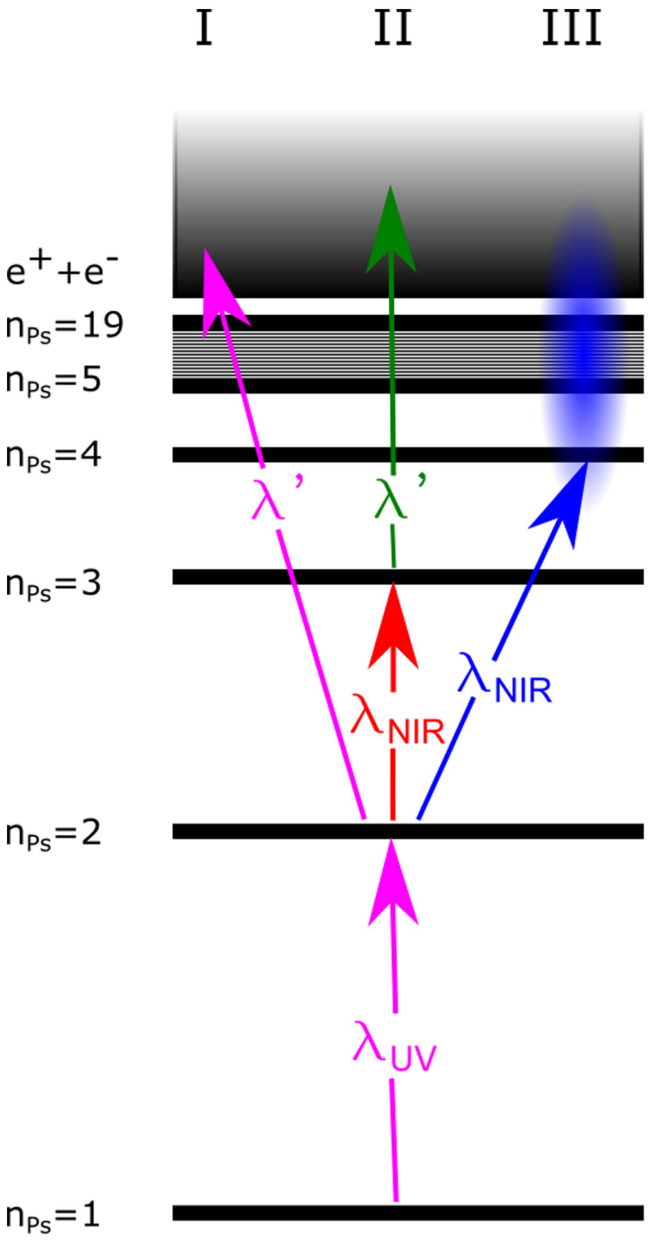

Figure 2. Simplified Ps energy level schematic with excitation channels highlighted. I Traditional $(1 + 1')$ Resonance-Enhanced MultiPhoton Ionisation, REMPI; Ps excitation and ionisation. II Traditional $(2 + 1')$ REMPI; doubly-resonant Ps excitation and ionisation. III Excitation of Ps to Rydberg states and the continuum.

3. Excitation of o-Ps to the 2P state

The gamma-rays emitted as a result of the Ps annihilations were detected, following Cassidy *et al* [37], using a $PbWO_4$ scintillator-phototube detector arrangement applied in the Single Shot Positron Annihilation Lifetime Spectroscopy

(SSPALS) mode. Here the output signal of the detector was recorded on a positron pulse shot-by-shot basis, and then integrated as required to give the SSPALS signal, $V(t)$. This signal is modelled through the convolution of a Gaussian time profile for the initially implanted positrons, a gamma emission function assuming an o-Ps production fraction with subsequent exponential decay, and a detector function approximated as a step function with exponential decay. A number of assumptions are inherent, such as crystal linearity, and that the annihilation of p-Ps and unconverted positrons, and the detector rise-time, are much faster than other timescales (i.e., essentially instantaneous). Further details can be found in [38], with use of the formula (see below) largely validated through Monte Carlo simulation by Deller [39]. Thus, the presence of o-Ps in vacuum is inferred by fitting $V(t)$ according to,

$$V(t) = \frac{A e^{-\left(\frac{1}{\tau_D}+\frac{1}{\tau_S}\right)t}}{2(\tau_D-\tau_S)} \times \left(e^{\left(\frac{t}{\tau_S}+\frac{2t_0\tau_D+\sigma^2}{2\tau_D^2}\right)}((2+S)\tau_D + 2(-1+S)\tau_S)\mathrm{Erfc}\left[\frac{t_0\tau_D-\tau_D t+\sigma^2}{\sqrt{2}\,\tau_D\sigma}\right] - 3e^{\left(\frac{t}{\tau_D}+\frac{2t_0\tau_S+\sigma^2}{2\tau_S^2}\right)}S\tau_D \times \mathrm{Erfc}\left[\frac{t_0\tau_S-\tau_S t+\sigma^2}{\sqrt{2}\,\tau_S\sigma}\right]\right). \quad (1)$$

Here A is the amplitude (related to the number of positrons striking the target), τ_D and τ_S are the detector signal decay time and characteristic o-Ps annihilation lifetime respectively, S is the free o-Ps fraction, σ is the temporal standard deviation of the incident positron cloud and t_0 the arbitrary time of the maximum of the SSPALS spectrum. Free fitting of equation (1) to a no-laser SSPALS spectrum resulted in $S \sim (27 \pm 1)\%$, $\tau_S \sim (174 \pm 18)$ ns, $\tau_D \sim (11.4 \pm 0.1)$ ns and $\sigma \sim (1.7 \pm 0.2)$ ns. At the positron implantation energy of 3 keV used in the present experiment it is expected [40] that nearly all the o-Ps produced in the silica sample is emitted into vacuum, such that the derived value for S is close to the vacuum fraction. Note that we have only used equation (1) to derive S directly—to obtain excitation efficiencies (and indirect values for S) we have used the delayed fraction analysis described below.

Following illumination with 243 nm light, the presence of $n_{Ps} = 2$ Ps (the 2P state) was identified in one of two ways, as illustrated in figure 3. In the first, a narrow time width peak, predominantly due to 2γ annihilations, was observed coincident with the application of the suitably tuned laser (see figure 3(a)). In this instance, the timing of the latter was chosen to be at least 50 ns after the primary peak (due to prompt positron annihilations following injection into the sample) such that the smaller second peak is clearly visible above the o-Ps long time 'tail'. This increase in 2γ signal was due to the presence of the magnetic field from the Nd magnet, which induced Zeeman mixing in the excited state followed by decay to the para-positronium ground state and prompt annihilation. In order to quantify the 2γ increase as a proxy for production of the 2P state we define a delayed fraction,

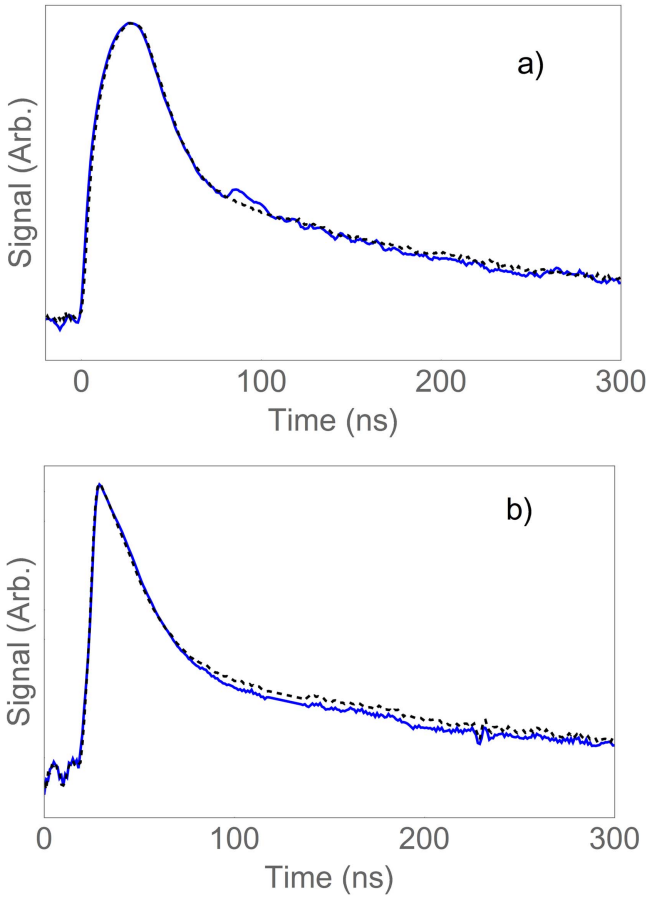

Figure 3. SSPALS traces, $V(t)$ showing (a) the Zeeman-quenched delayed peak (around 90 ns) and (b) the depressed o–Ps signal (after ~90 ns) due to the prompt quenched 2P population. The dashed line is the trace for no laser present. See text for details.

f_d, as [41]

$$f_d = \frac{\int \mathrm{Ps}^* \text{ signal}}{\int \text{total}}, \quad (2)$$

where $\int \mathrm{Ps}^*$ signal is the time region of the SSPALS spectrum containing the signal of interest and $\int$total is the full integrated SSPALS spectrum. (Note that the integration time limits are to some extent arbitrary, and are contingent upon experimental circumstances: e.g., positron and laser pulse widths.) This allows the fractional excess, f_{ex}^{1S-2P}, due to excitation to the 2P state to be computed as

$$f_{ex}^{1S-2P} = \frac{(f_d[\mathrm{UV}] - f_d[\mathrm{No}])}{f_d[\mathrm{No}]}, \quad (3)$$

where [UV] and [No] are with and without the 243 nm laser respectively. For the data shown in figure 3(a) $f_{ex}^{1S-2P} = 19 \pm 1\%$.

The second manner by which the presence of 2P Ps can be deduced is by the disappearance of 3γ signal from the SSPALS 'tail' when the timing of the lasers is arranged such that the beams arrive approximately 10 ns after the positron ensemble strikes the sample. Here the 2γ increase is buried in

the prompt peak, with the concomitant loss of long-lived o-Ps shown in an example spectrum in figure 3(b). In order to quantify this signal we use a similar definition to equation (3) for the reduced o-Ps signal which results in $f_{\rm ex}^{\rm 1S-2P} = 7.3 \pm 0.6\%$ for the spectra shown in figure 3(b).

It should be noted that for the magnetic quenching data presented in figure 3, a 1–2 kVcm^{-1} electric field was present within the laser beam–Ps cloud interaction region as a result of the acceleration bias applied to the SiO_2 target (with the grid electrically grounded: see figure 1). However, due to concerns regarding the effects of this field (e.g., Stark mixing and ionisation) on Rydberg Ps produced in subsequent experiments (see below), the field was reduced to $\lesssim$5 V cm^{-1} by applying a voltage to the grid close to that at which the target was held.

The underlying quenching process used for the work described above relied upon the presence of a permanent magnet located outside the vacuum chamber to increase the measured local magnetic field at the laser beam–Ps cloud interaction region to ~20 mT, which in turn enhanced the Zeeman mixing of the Ps states and significantly reduced the radiative decay lifetime. To excite the $n_{\rm Ps} = 2$ Ps further it was therefore beneficial, where possible, to suppress this mixing to increase the laser beam–Ps cloud interaction time, and as such the permanent magnet was removed (leaving the ~8 mT guiding field).

With reduced Zeeman mixing another mechanism to promote positron annihilation is required to confirm excitation to $n_{\rm Ps} = 2$ and so the second OPO was used to generate an 8 ns, $\leqslant$60 mJ, pulse near the ionisation threshold at around 729 nm, which was directed into the Ps cloud coincident with the 243 nm radiation to liberate the positrons by photoionisation. Figure 4(a) illustrates the resultant secondary prompt annihilation peak (similar to that of figure 3(a)) caused by the free positrons being directed back to strike the SiO_2 sample and annihilating there at the surface. Due to the low incident energy of $\lesssim$5 eV, little additional Ps is likely to be formed (see e.g. [29], figure 6), and the visible loss of 3γ o-Ps signal allows S to be evaluated as ~28% (via $S \sim 1.8(f_{\rm d} - 1)$ for our system as detailed in [27]) for the data presented in figure 4(a).

When the quench and ionisation based techniques are operated consecutively, or interleaved, we observe that the S values, as calculated from the detection of the secondary prompt annihilation peak using the delayed fraction, are very similar, and in accord with the no-laser SSPALS fit, and therefore the two techniques can be considered complementary. From this we infer that the photoionisation transition is saturated with an efficiency close to unity, as found from ionisation from the 3P state by Aghion *et al* [22].

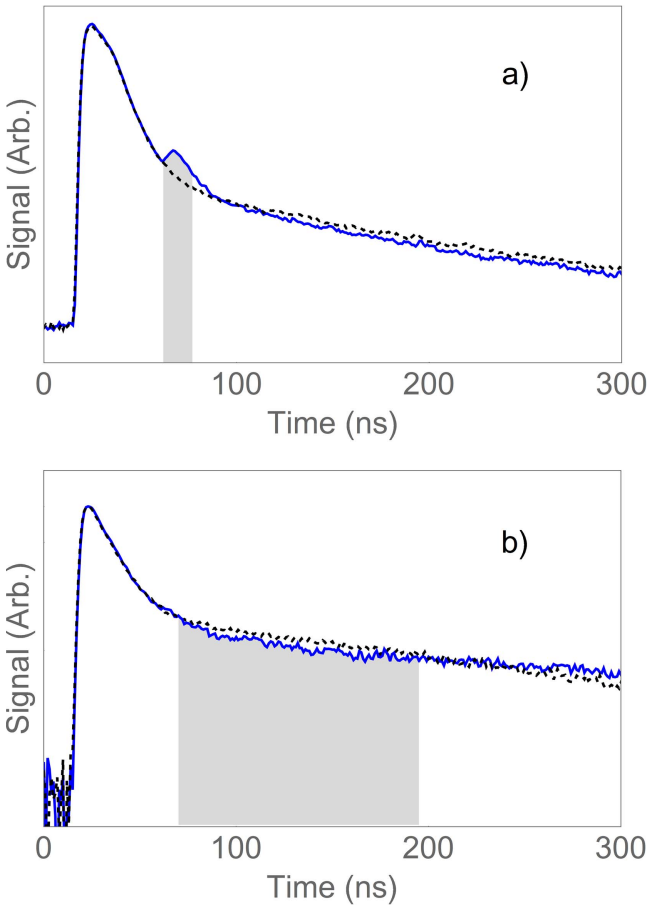

Figure 4. SSPALS trace showing the positron annihilation signal caused by photoionisation from the (a) $n_{\rm Ps} = 2$ state and (b) $n_{\rm Ps} = 13$ state, with in both cases the dashed lines corresponding to no lasers present. The time windows used to derive the delayed fractions are identified by shaded regions in each case. Further details on the features of the spectra and their analysis can be found in the text.

4. Resonance-enhanced multiplephoton ionisation for $n_{\rm Ps} = 3-5$

As discussed in section 2.2, and illustrated in exitation path II of figure 2, for excitation to higher $n_{\rm Ps}$ levels, the wavelength of the second OPO is suitably tuned and as a result the two output wavelengths are correlated such that $\lambda_{\rm NIR} + \lambda' = 532$ nm. In this way the $n_{\rm Ps} = 2$ o-Ps is excited and subsequently ionised, and the second narrow (in time) annihilation peak is detected (as discussed in section 3). If the wavelength of either the ultraviolet or the infra-red laser is off resonance or absent, the second peak is not observed. In order to quantify this signal a similar parameter to that presented by Cassidy *et al* [27] is used. However, our definition is somewhat modified due to the lack of a quench signal, but the physical description of this parameter is unchanged, namely the fraction of $n_{\rm Ps} = 2$ o-Ps that has been ionised following excitation into a higher state. Thus, we define this excitation fraction as

$$f_{\rm ex}^{\rm 2P-n_{Ps}} = \frac{f_{\rm d}\,[\rm No] - f_{\rm d}\,[\rm UV + IR]}{f_{\rm d}\,[\rm ion]\,f_{\rm d}\,[\rm No]}, \qquad (4)$$

where $f_{\rm d}$, is defined as in equation (2) and [No], [UV+IR] and [ion] utilise no lasers and three and two appropriately tuned lasers respectively. The fraction $f_{\rm d}\,[\rm ion]$ is that due to direct (quasi-resonant) photoionisation close to 729 nm from the 2P level, and with this (and the photoionisation from the Rydberg level), occurring with unity efficiency, the probability of 1S-2P

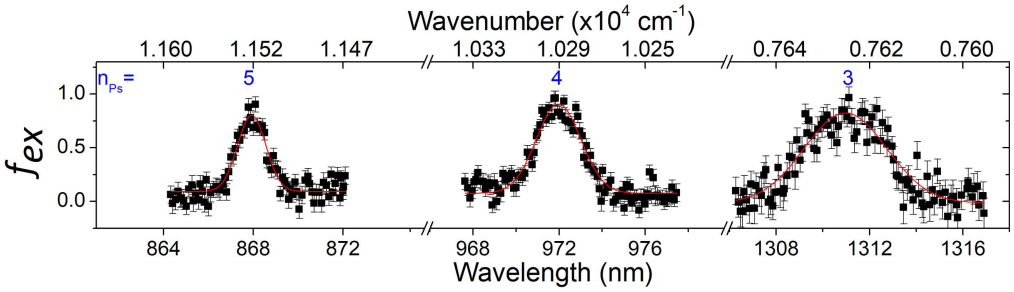

Figure 5. Excitation fraction following Resonance-Enhanced MultiPhoton Ionisation (REMPI) for states $n_{Ps} = 3$, 4 and 5. The fitted lines are Gaussians.

excitation is removed to give the required excitation fraction. It should be noted that [No] measurements were interleaved for each wavelength measurement, whereas the [ion] measurement was taken intermittently throughout the scan. The values of f_d for the latter typically varied by $\lesssim$0.5% and the mean over an appropriate range was used for [ion]. Figure 5 illustrates the efficiency of exciting o-Ps to the 2P state, followed by excitation to a higher state (n_{Ps}= 3, 4, or 5) and subsequent ionisation with efficiency of ~80%. Unfortunately, since the OPO wavelengths are correlated, states higher than $n_{Ps} = 5$ are not accessible using this method since there was insufficient power available at the long wavelengths λ' (idler wave of the OPO) required for ionisation. In order to access higher lying states the detection technique was modified, as described in the following section, to take advantage of the variations in the aforementioned SSPALS o-Ps 'tail'.

5. Excitation of o-Ps to Rydberg states

Following irradiation with 243 nm light and the concomitant excitation to $n_{Ps} = 2$, the second OPO laser was tuned to an appropriate wavelength for further excitation, and SSPALS measurements undertaken as the laser was scanned across a particular transition line. Schematically this process is illustrated in excitation path III of figure 2 and SSPALS plots for interleaved spectra with lasers on and off are shown in figure 4(b) for the case of $n_{Ps} = 13$. When excitation to the high-lying level occurs, the o-Ps lifetime is extended, such that the laser on curve initially dips below that for laser off, only to recover and exceed the latter at later times. The excitation signal is derived by setting an appropriate time window to compare the on–off f_d values in the 'dip' region to compute an excess parameter similar to those described in section 3. As for the REMPI results described in section 4, these data are normalised for the 2P yield using measurements of f_d [ion] taken before and after each Rydberg line scan. There is some ambiguity here, since the REMPI measurements entail detection of 2 γ-ray events due to positron annihilation in the target, whilst the Rydberg signal involves, predominantly, 3γ events due to o-Ps decay. Figure 6 shows the resulting fractional excess as the second OPO wavelength was varied between 975 and 726 nm, whilst figure 7 shows a subset of the data from $n_{Ps} = 14$ to ionisation. The presence of peaks indicate that the Ps was first excited to the $n_{Ps} = 2$ and subsequently to a higher, longer lived, state.

The poor resolution of states above $n_{Ps} = 18$, as illustrated in figures 6 and 7, is predominantly due to the effects of the bandwidth of the excitation lasers, and laser-induced power broadening. The bandwidths of the UV and NIR lasers are assumed to be the same (at 225 GHz, see section 2.2), resulting in a Gaussian convoluted bandwidth for the combined excitation of around 320 GHz. This figure will be increased by power broadening, and it is plausible to take the observed level width data at high n_{Ps}, as displayed in figure 8, as a measure of the effective bandwidth for the transitions into the Rydberg states. This amounts to around 360 GHz, or 12 cm^{-1}. There will be further contributions from Stark and Zeeman effects, which will become more important as n_{Ps} is raised. For comparison we can estimate the Rydberg level spacing (from the 1st-order formula for Ps) to be around 20 cm^{-1} for n_{Ps} = 17–18, and is already below the effective bandwidth for the $n_{Ps} = 21$ and 22 states.

The aforementioned effects are not fundamental limitations as excitation to $n_{Ps} = 35$ is routinely observed by others [42]. It should be noted that Cassidy *et al* [27] have also observed behaviour similar to that shown at the shorter wavelengths in figures 6 and 7 and attributed it to system-specific effects, such as field ionisation and the influence of the motional Stark effect. Given the differences in the experimental apparatus and techniques it is likely that details of the interaction between the external **E** and **B** fields, the o-Ps and the interaction lasers contributes to this behaviour in our case.

The correlation between the onset of Ps ionisation and excitation as the 2nd excitation laser is tuned to wavelengths below ~733 nm can be seen in figure 7 (a subset of figure 6), in which the integration windows used in determining f_d from equation (2) were modified to interrogate the appearance signal illustrated in figure 3(a) as opposed to the disappearance of signal illustrated in figure 3(b). The appearance of ionised Ps at, and below, 733 nm is likely due to the aforementioned convoluted laser linewidth and the presence of motional field effects, which are known to lower the threshold for ionisation (see, e.g., [21]).

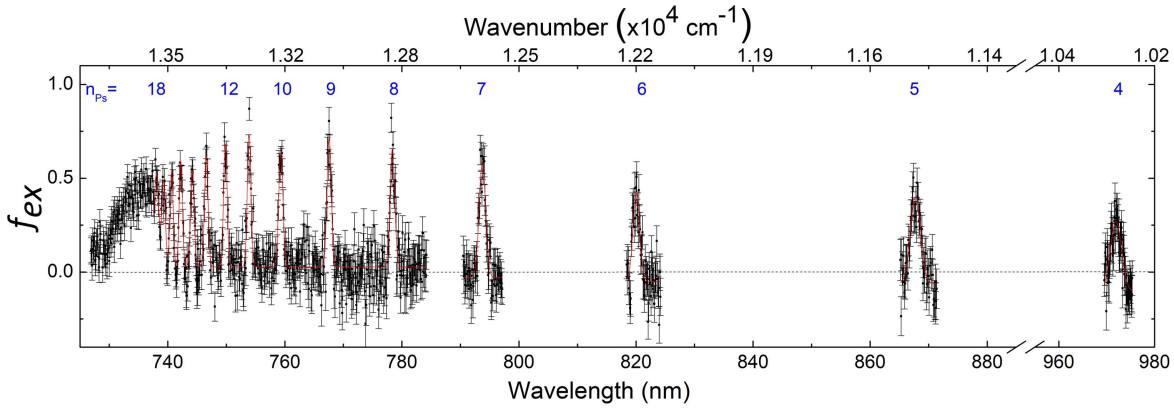

Figure 6. Excess of signal within a specified window of the SSPALS spectra relative to the corresponding no laser SSPALS spectra for multiple wavelengths of the 2nd excitation laser. These wavelengths correspond to n_{Ps} states 4–18. Gaussians are fitted to the resolvable peaks.

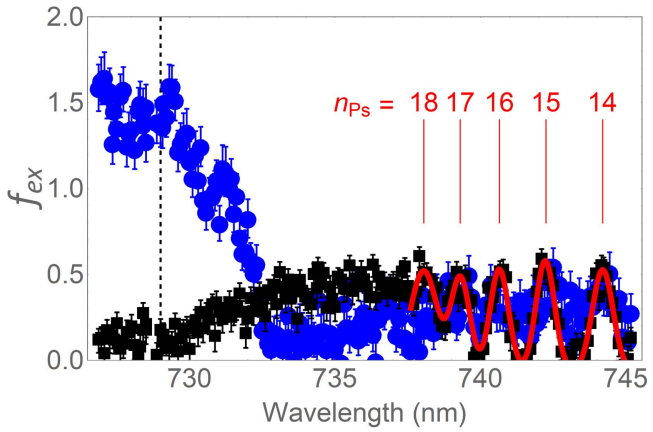

Figure 7. A subset of figure 6 showing $n_{Ps} = 14$ to vacuum (■) with Gaussian fits (–) and the corresponding excess of 2γ's signifying ionisation (●) (following the use of a modified time region for f_d). See text for details. The ionisation threshold at 729 nm is shown as the dashed vertical line.

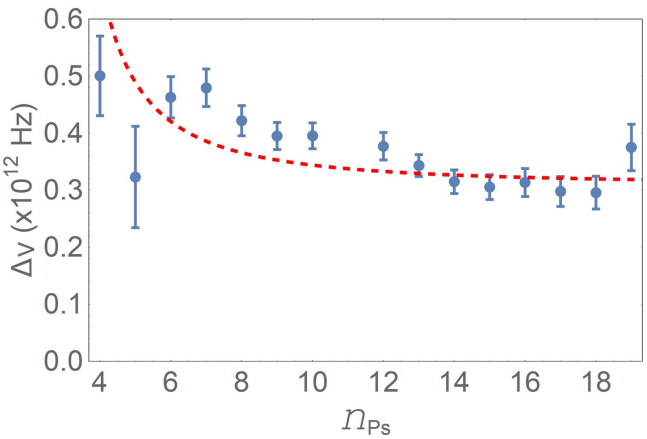

Figure 8. Level width data (for the lines shown in figure 6) rescaled to frequency, $\Delta\nu$. The calculated linewidth due to power broadening [43] convolved with OPO linewidth (of around 11 cm^{-1}) for a pulse energy of 10 mJ (– –).

6. Excitation efficiencies

We can use the results of the data presented in sections 4 and 5 to provide estimates of the efficiency of excitation of o-Ps from the ground state to the 2P state by cross-normalising the REMPI and Rydberg data. From the data presented in figure 6, when analysed without normalisation to f_d [ion], $9 \pm 2\%$ of all o-Ps produced is excited to $n_{Ps} = 4$ and from figure 5, $80 \pm 5\%$ of all $n_{Ps} = 2$ o-Ps is excited to $n_{Ps} = 4$ and subsequently ionised. Assuming unity efficiency for ionisation (which is reasonable since the 2P quench and ionisation results are identical), we can estimate that $11 \pm 2\%$ of all o-Ps is excited to $n_{Ps} = 2$. An identical treatment of $n_{Ps} = 5$ suggests the efficiency is $15 \pm 3\%$, and a similar conclusion can be drawn for states with $n_{Ps} > 5$. Although this range is relatively large it is not unreasonable since the perpendicular Doppler-linewidth overlap is ~30%, the emitted Ps cloud is spatially divergent, and caution dictated that we have a rather large separation (~2 mm) between the silica sample and laser edge. This results in only a subset of all available o-Ps being interrogated.

7. Concluding remarks

The emission of ortho-positronium into vacuum from a nanoporous SiO_2 sample following bombardment by positrons ejected from a two-stage buffer gas accumulator has once again been shown to be efficient and reliable. The ortho-positronium has been excited from the ground state to ionisation with intermediate levels $2 \leqslant n_{Ps} \leqslant 18$ clearly addressable. Access to states with $n_{Ps} > 18$ is also likely to be possible, but they are not currently resolved within our system. While >80% efficiency is achievable for excitation from $n_{Ps} = 2$, the initial Lyman-α transition appears to be the current limiting step with the bulk of data reported herein attaining $\epsilon^2_{ex} = 9\%$–18% but $\epsilon^2_{ex} = 40\%$ efficiencies have been observed elsewhere. With the minor modifications necessary to improve this, particularly related to the spatial

location of the laser beam path relative to the silica sample and the attendant laser timing modification, the excitation efficiency of 1S o-Ps to $n_{Ps} \leqslant 18$ is expected to be ~30%.

The principal quantum number states of positronium presented in this paper, $n_{Ps} = 2$–18, have been addressed by the use of a fully automated solid state commercial laser system that requires minimal user intervention or expertise and is thus significantly easier to use than alternative laser systems. The simplification of the laser equipment and the subsequent ease with which excited positronium can be produced should enable its uses in areas that were previously inaccessible to non-specialists. One such area is to increase the efficient state-selective production of antihydrogen (where the formation cross section is expected to increase with n_{Ps}) for spectroscopy [44, 45] or gravity measurements [23, 24, 46].

Further improvements to this technique are desirable, such as increasing the flux of implanted positrons, enhancing the positron to ortho-positronium conversion efficiency while maintaining the high (almost unity) emission efficiency to vacuum and increasing the 2P-laser linewidth overlap with the Doppler broadened 243 nm line.

Acknowledgments

The authors would like to thank the EPSRC (UK) and The Leverhulme Trust for funding, and past members of the group, and in particular Drs Adam Deller and Tim Mortensen. We are grateful for the enthusiastic support given to us by the College of Science technical staff team.

ORCID iDs

C J Baker https://orcid.org/0000-0002-9448-8419
C A Isaac https://orcid.org/0000-0002-7813-1903

References

[1] Mohorovičić S 1934 *Astron. Nachr.* **253** 93
[2] Deutsch M 1951 *Phys. Rev.* **82** 455
[3] Chu S, Mills A P Jr and Hall J L 1984 *Phys. Rev. Lett.* **52** 1689
[4] Fee M S, Mills A P Jr, Chu S, Shaw E D, Danzmann K, Chichester R J and Zuckerman D M 1993 *Phys. Rev. Lett.* **70** 1397
[5] Fee M S, Chu S, Mills A P Jr, Chichester R J, Zuckerman D M, Shaw E D and Danzmann K 1993 *Phys. Rev.* A **48** 192
[6] Ziock K P, Dermer C D, Howell R H, Magnotta F and Jones K M 1990 *J. Phys. B: At. Mol. Opt. Phys.* **23** 329
[7] Jones A C L, Hisakado T H, Goldman H J, Tom H W K, Mills A P Jr and Cassidy D B 2014 *Phys. Rev.* A **90** 012503
[8] Brawley S J, Armitage S, Beale J, Leslie D E, Williams A I and Laricchia G 2010 *Science* **330** 789
[9] Brawley S J, Fayer S E, Shipman M and Laricchia G 2015 *Phys. Rev. Lett.* **115** 223201
[10] Laricchia G and Walters H R J 2012 *La Riv. Nuovo Cimento* **35** 305
[11] Cassidy D B, Yokoyama K T, Deng S H M, Griscom D L, Miyadera H, Tom H W K, Varma C M and Mills A P Jr 2007 *Phys. Rev.* B **75** 085415
[12] Dlubek G, Fretwell H M and Alam M A 2000 *Macromolecules* **33** 187
[13] Roussenaov M V and Alam M A 2013 *J. Phys. Conf. Ser.* **443** 012044
[14] Mills A P Jr and Leventhal M 2002 *Nucl. Instrum. Methods* B **192** 102
[15] Cassidy D B and Hogan S D 2014 *Int. J. Mod. Phys.: Conf. Ser.* **30** 1460259
[16] Crivelli P, Cooke D A and Friedreich S 2014 *Int. J. Mod. Phys.: Conf. Ser.* **30** 1460257
[17] Humberston J W, Charlton M, Jacobsen F M and Deutch B I 1987 *J. Phys. B: At. Mol. Phys.* **20** L25
[18] Charlton M 1990 *Phys. Lett.* A **143** 143
[19] Deutch B I, Charlton M, Holzscheiter M H, Hvelplund P, Jørgensen L V, Knudsen H, Laricchia G, Merrison J P and Poulsen M R 1993 *Hyperfine Interact.* **76** 153
[20] Storry C H *et al* (ATRAP Collaboration) 2004 *Phys. Rev. Lett.* **93** 263401
[21] Castelli F, Boscolo I, Cialdi S, Giammarchi M G and Comparat D 2008 *Phys. Rev.* A **78** 052512
[22] Aghion S *et al* (AEgIS Collaboration) 2016 *Phys. Rev.* A **94** 012507
[23] van der Werf D P 2014 *Int. J. Mod. Phys.: Conf. Ser.* **30** 1460263
[24] Krasnický D *et al* (AEgIS Collaboration) 2014 *Int. J. Mod. Phys.: Conf. Ser.* **30** 1460262
[25] Kadyrov A S, Rawlins C M, Stelbovics A T, Bray I and Charlton M 2015 *Phys. Rev. Lett.* **114** 183201
[26] Rawlins C M, Kadyrov A S, Stelbovics A T, Bray I and Charlton M 2016 *Phys. Rev.* A **93** 012709
[27] Cassidy D B, Hisakado T H, Tom H W K and Mills A P Jr 2012 *Phys. Rev. Lett.* **108** 043401
[28] Clarke J, van der Werf D P, Griffiths B, Beddows D C S, Charlton M, Telle H H and Watkeys P R 2006 *Rev. Sci. Inst.* **77** 063302
[29] Deller A, Edwards D, Mortensen T, Isaac C A, van der Werf D P, Telle H H and Charlton M 2015 *J. Phys. B: At. Mol. Opt. Phys.* **48** 175001
[30] Mills A P Jr and Gullikson E M 1986 *Appl. Phys. Lett.* **49** 1121
[31] Khatri R, Charlton M, Sferlazzo P, Lynn K G, Mills A P Jr and Roellig L O 1990 *Appl. Phys. Lett.* **57** 2374
[32] van der Werf D P, Isaac C A, Baker C J, Mortensen T, Kerrigan S J and Charlton M 2012 *New J. Phys.* **14** 075022
[33] Notte J and Fajans J 1994 *Phys. Plasmas* **1** 1123
[34] Greaves R G and Moxom J M 2008 *Phys. Plasmas* **15** 072304
[35] Isaac C A, Baker C J, Mortensen T, van der Werf D P and Charlton M 2011 *Phys. Rev. Lett.* **107** 033201
[36] Liszkay L *et al* 2008 *Appl. Phys. Lett.* **92** 063114
[37] Cassidy D B, Deng S H, Tanaka H K M and Mills A P Jr 2006 *Appl. Phys. Lett.* **88** 194105
[38] Deller A 2013 Positron accumulation and laser excitation of the positronium atom *PhD Thesis* Swansea University
[39] Deller A 2016 arXiv:1609.04993
[40] Liszkay L 2016 private communication
[41] Cassidy D B and Mills A P Jr 2007 *Nature* **449** 195
[42] Jones A C L, Hisakado T H, Goldman H J, Tom H W K, Mills A P Jr and Cassidy D B 2014 *Phys. Rev.* A **90** 012503
[43] Foot C J 2005 *Atomic Physics* (Oxford: Oxford University Press)
[44] Amole C *et al* (ALPHA Collaboration) 2012 *Nature* **483** 439
[45] Ahmadi M *et al* (ALPHA Collaboration) 2017 *Nature* **541** 506
[46] Amole C *et al* (ALPHA Collaboration) 2013 *Nat. Commun.* **4** 1875